Far-Field Laser Intensity Drop-Outs Caused by Turbulent Boundary Layers

Stanislav Gordeyev, Jacob Cress and Eric Jumper,
Department of Aerospace and Mechanical Engineering,
University of Notre Dame, Notre Dame, IN 46556

Usually aero-optical effects are quantified in time-averaged manner, like time-averaged OPD_{rms} or time-averaged Strehl Ratio (SR) on a target. However, for airborne free-space laser-based communication systems instantaneous SR should be studied as well. An attached transonic boundary layer, for example, provides a relatively-high time-average SR; however, experimentally it was discovered that it has many sharp intensity dropouts, which typically last for several milliseconds. Left untreated, these drop-outs lead to significant data loss, disrupting and slowing down airborne laser-based communications. This paper presents experimentally-measured instantaneous near-field wavefront statistics due to laser transmission through subsonic boundary layers. The resulting far-field SR for different flow conditions and apertures sizes are also presented. Using scaling laws for boundary layers, a simple relation between flight conditions and the relative amount of time when the SR drops below a prescribed threshold is developed, this model leads to the development of a method for predicting system performance for a free-space communication system. This method is discussed along possible approaches to using it for designing and optimizing current and future laser-based communication systems.

Keywords: boundary layer, communication, laser

Nomenclature

Ap	=	laser beam aperture
$CCDF$	=	Complimentary Cumulative Distribution Function
C_f	=	local skin friction coefficient
F_1	=	function, defined in (3)
K_{DG}	=	Gladstone-Dale constant
M	=	Mach number
m	=	temporal mean of the natural log of $OPD_{rms}(t)$
n'	=	fluctuating component of the index of refraction
OPD	=	Optical Path Difference
OPD_{rms}	=	spatial root-mean-square of OPD
OPD_{norm}	=	normalized OPD, as defined in (6)

OPD_{rms}^{norm}	=	spatial root-mean-square of OPD_{norm}
OPL	=	Optical Path Length
PDF	=	Probability Density Function
q	=	dynamic pressure
r_2	=	ratio between the bulk and free-stream temperatures
SR	=	Strehl Ratio
s	=	temporal standard deviation of the natural log of $OPD_{\text{rms}}(t)$
t	=	time
TH	=	threshold value
TH_{SR}	=	Strehl Ratio threshold value
U_c	=	convection velocity
x, y, z	=	coordinate system
γ	=	viewing angle
δ	=	boundary-layer thickness
δ^*	=	boundary-layer displacement thickness
λ	=	laser wavelength
μ	=	spatial time-averaged root-mean-square of OPD_{norm}
ρ	=	freestream density
ρ'	=	density fluctuations
ρ_{SL}	=	see-level density, $\rho_{\text{SL}} = 1.225$ kg $\cdot$ m^{-3}
θ	=	deflection angle or jitter
Σ	=	standard deviation or the spread of the $OPD_{rms}^{norm}(t)$
overbar	=	time averaging

I. Boundary-layer aero-optical effects

Laser-based, free-space communication systems have the potential of providing very-high bandwidth, secure lines of communications from air-to-air, air-to-ground and air-to-satellite. Because of its nominal large field-of-regard turrets are used to direct the laser beam toward its target/receiver. Unfortunately, turrets create significant turbulent wakes and therefore variable index-of-refraction downstream of the turret, which significantly disrupts the outgoing laser beam and, in effect, obscures a significant portion of the field-of-regard, even at moderate speeds well below transonic [1]. These so-called aero-optical effects [2,3] are typically quantified by the Optical Path Difference, or *OPD(x,y,t)*, over the beam aperture after passing through the turbulent region defined as,

$$OPD(x,y,t) = \int_0^{\delta} n'(x,y,z,t)dz = K_{GD}\int_0^{\delta} \rho'(x,y,z,t)dz \qquad (1)$$

where n' is the index-of-refraction, ρ' is the density fluctuation field, K_{DG} is the Gladstone-Dale constant, δ is the thickness of the turbulent region and the z-direction is aligned along the beam propagation direction. The level of aero-optical aberrations are usually described by the spatial root-mean-square of *OPD*, $OPD_{\text{rms}}(t)$.The far-field intensity for a large-aperture beam is usually characterized by a Strehl Ratio, *SR*, which is defined the actual on-axis light irradiance in the far field divided by the diffraction-limited irradiance. In general, both the diffraction-limited and the actual distorted beam irradiance in the far field can be calculated using the Fraunhofer approximation [4].

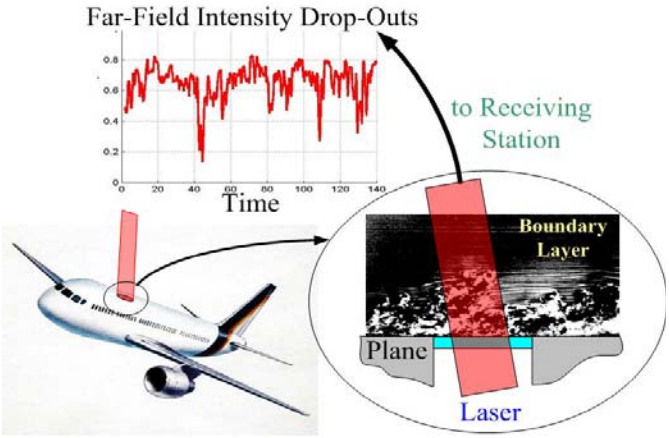

Figure 1. Conceptual turret-free laser-based communication system and boundary-layer-related intensity drop-outs.

To avoid large aero-optical effects caused by turrets, system designers have considered placing the pointing-and-tracking turret completely inside of the aircraft, avoiding the problem of separated flow, see Figure 1. Still, the outgoing beam has to pass through a turbulent boundary layer always present on the skin of the aircraft. Density variations inside the compressible boundary layer were found to distort the outgoing beam, resulting in significant intermittent increases in OPD_{rms} and subsequent intensity drop-outs in the far-field at the receiver [5,6]. These high-frequency drop-outs, if unchecked, result in data loss during these drop-outs, inevitably slowing down or even completely disrupting the high-bandwidth data transmission; this is especially true for transonic and supersonic flight speeds.

Aero-optical properties of turbulent boundary layers have been investigated since mid-1950s. The first investigation was by Liepmann [7] and made use of the jitter angle of a thin beam of light as it traveled through the compressible, turbulent boundary layers on the sides of high-speed wind tunnels as a way to quantify the crispness of Schlieren photographs. Stine & Winovich [8] performed photometric measurements of the time-averaged radiation field at the focal plane of a receiving telescope; their work raised the prospect of using optical degradation measurements as a method of inferring turbulence scales. An important analytical tool in studying the aero-optical problem in general was the linking equation, developed by Sutton [9,10]. The equation relates the statistical properties of the turbulent flow to aero-optical distortions. For boundary layers, the average pressure fluctuations are several times smaller than temperature fluctuations [11] so that density fluctuations are at least statistically related to temperature fluctuations only. Under the presumption of negligible pressure fluctuations, these temperature fluctuations, in the case of an adiabatic wall, can be directly calculated from velocity fluctuations using the Strong Reynolds Analogy (SRA) [12]. Rose [13] used the linking equation with these assumptions to estimate aero-optical distortions caused by subsonic turbulent boundary layers by measuring velocity profiles and found that aero-optical distortions scaled as, $OPD_{\text{rms}} \sim q\delta$, where q is the dynamic pressure and δ is the boundary-layer thickness. Gilbert [14] performed direct, although time-averaged, aero-optical measurements using an interferometer and, compared his results with Rose's data, somewhat validating the linking equation for boundary layers. Masson [15] did a more careful examination of Gilbert and Rose data and proposed a correction to the linking equation that gave a better comparison; however, his conclusion was similar to Gilbert's, that the linking equation is essentially valid.

Development of accurate high-speed wavefront sensors, such as the Malley probe [16] and high-speed Shack-Hartmann sensors allow now direct and accurate measurements of time and space-resolved aero-optical aberrations. Based on these measurements, it has now been firmly established that the structures responsible for aero-optical aberrations in the boundary-layer travel at approximately 0.8 to 0.85 of the freestream speed and have streamwise length of the order of several boundary-layer thicknesses [5,17]. These and other preliminary conditional

measurements [18,19] place the origin of aero-optical structure in the outer region of the boundary layer.

Over the last few years several statistical-based models to predict the time-averaged aero-optical distortions of turbulent boundary layers have been developed. Based on extensive aero-optical boundary-layer measurements at different subsonic speeds, M, boundary-layer thicknesses and viewing angles, γ, [20,5] the boundary-layer aero-optical aberrations for large apertures were found to be

$$OPD_{rms} = 1.7 \cdot 10^{-5} (\rho / \rho_{SL}) M^2 \delta^* / \sin(\gamma), \quad (2)$$

where ρ and ρ_{SL} are the freestream and the sea-level densities, respectively, M is the freestream Mach number and δ^* is the boundary-layer displacement thickness. Based on the measurements in transonic and hypersonic boundary layers, Wyckham & Smits [21] proposed the scaling relation $OPD_{rms} \sim \rho M^2 \delta \sqrt{C_f} r_2^{3/2}$, where C_f is the local skin friction coefficient and r_2 is the ratio between the bulk and free-stream temperatures ($r_2 \approx 1$ at subsonic speeds). Gordeyev et al. [17] used the linking equation along with the assumptions of negligible pressure fluctuations and the SRA to predict $OPD_{\rm rms}$ at transonic and supersonic speeds for different Reynolds numbers and they found that

$$OPD_{rms} = 0.2 K_{GD} \rho \delta \sqrt{C_f} F_1(M), \quad (3)$$

where $F_1(M) \approx M^2$ at subsonic speeds. Both models [21] and [17] were found to generally agree with each other up to $M = 5$ and, at limit of subsonic speeds, they can be reduced to (2). Extensions for subsonic turbulent boundary layers with non-adiabatic, heated/cooled walls were presented in [5,22].

This paper is focused on the temporal statistics of the aero-optical distortions of subsonic turbulent boundary layers and develops the statistical-based approach to predict the relative amount of the far-field intensity drop-outs. Section II describes the experimental set-up, Section III describes the data reduction technique and the data analysis of $OPD_{\rm rms}(t)$ for different mach numbers and apertures. The method of calculating a relative duration of the intensity drop-outs for different flight conditions is also presented and illustrated. Finally, in the last Section conclusions are summarized.

II. Experimental Set-Up

The experiments were conducted in the Subsonic Wind Tunnel facility at the United States Air Force Academy in Colorado Springs, Colorado. A detailed description of the experimental facilities and an experimental procedure can be found in [5,20] and only essential details will be provided in this paper. The closed-loop tunnel has a test section 2.4 m long with a cross-sectional area of 0.9 m by 0.9 m. The boundary layer on the tunnel walls was approximately 25 mm thick. To measure instantaneous aero-optical distortions caused the subsonic boundary layer a highly-sensitive wavefront sensor called a Malley probe [16] was used. A schematic of the optical set up using the Malley probe is shown in Figure 2, left plot. Two parallel, small-aperture laser beams were traversed through the turbulent flow with boundary layers on the tunnel walls and were reflected back along the same path using the return mirror. The returning beams were split off and the jitter signal from each returning beam was measured with a Position Sensing Device, or *PSD*.

To eliminate the effect of the boundary layer on the opposite wall an optical insert was used. The narrow optical insert, shown in Figure 2, right picture, was protruded into the boundary layer flow and effectively allowed the Malley-probe laser beams to by-pass the boundary layer on the

opposite tunnel wall, see Figure 2, left plot. The length of the insert in the streamwise direction was 250 mm, it was 5 mm thick and was protruding 40 mm into the test section; the insert was capped with an optically transparent Plexiglas plate 5 mm thick. For the single boundary layer tests with the optical insert, the tested viewing angles were 48, 90, 124 and 133 degrees. In this paper only the results for 90 degrees will be reported. The tests were performed for incoming Mach numbers of 0.4 and 0.5. Data were sampled at 100 kHz for 30 seconds.

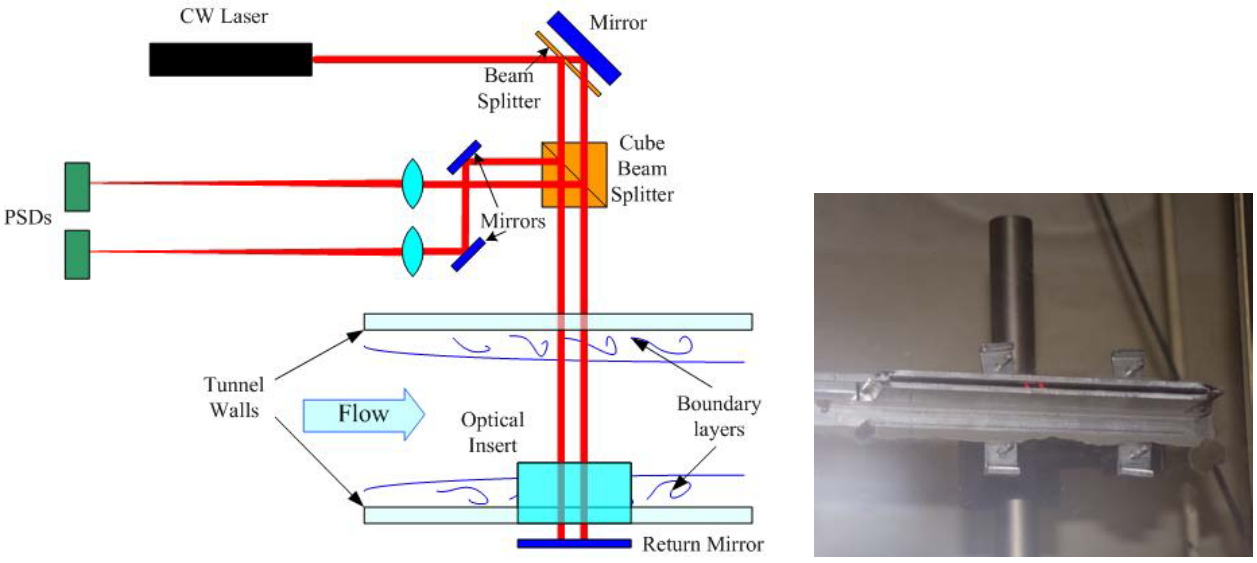

Figure 2: Left: Schematic of the Malley probe, single boundary layer set-up. Right: Optical Insert.

III. Results

A. Data reduction

The Malley probe is an optical sensor based upon the technique introduced by Malley et al. [23]. The operation of this instrument, which is described in detail in [16], assumes from Huygens' Principle that a small-aperture beam which passes through a variable index-of-refraction field will emerge from that region perpendicular to the wavefront of a larger beam propagated through the same location at the same moment. Therefore, a time-record of the deflection of the small-aperture beam gives a history of the wavefront slope at that location. If the convection velocity, U_c, of the aberrating structures is known, the *OPD* can be found using,

$$\begin{aligned} OPL(t) &= -U_c \int_{t_0}^{t} \theta(t)dt \\ OPD(t) &= OPL(t) - \overline{OPL(t)} \end{aligned}, \tag{4}$$

where *OPL* is the optical path length, $\theta(t)$ is the time series of the deflection angle and the overbar denotes the time-averaging. Using the frozen flow assumption, the 1-dimensional slice of the wavefront as a function of time and the streamwise direction can be found,

$$OPD(t) \rightarrow OPD(t - x/U_c) \tag{5}$$

Instead of estimating the convection velocity, as done by Malley et al [23], the inclusion of the second beam allows the convection velocity to be directly calculated [16]. The jitter signals

are correlated in the Fourier domain and the phase relation between the two beams, as a function of frequency, is determined. For a known separation between the two beams, the convection velocity can be found from the slope of the phase/frequency plot, see [16] for a detailed explanation.

The reconstruction procedure can be described as follows:

1. The reconstructed wavefront (5), see Figure 3(a), was divided into blocks corresponding to a given aperture, *Ap*, as shown in Figure 3(b).
2. Spatial piston (mean) and tip (slope) were removed from the wavefront for each aperture; Figure 3(c).
3. The *spatial* root-mean-square of the optical aberrations, $OPD_{\text{rms}}(Ap)$, was calculated for each aperture, resulting in a time series of $OPD_{\text{rms}}(Ap,t)$, see Figure 3(d).
4. The time-averaged spatial root-mean-square, $\overline{OPD_{rms}(Ap)}$, was calculated for each aperture.

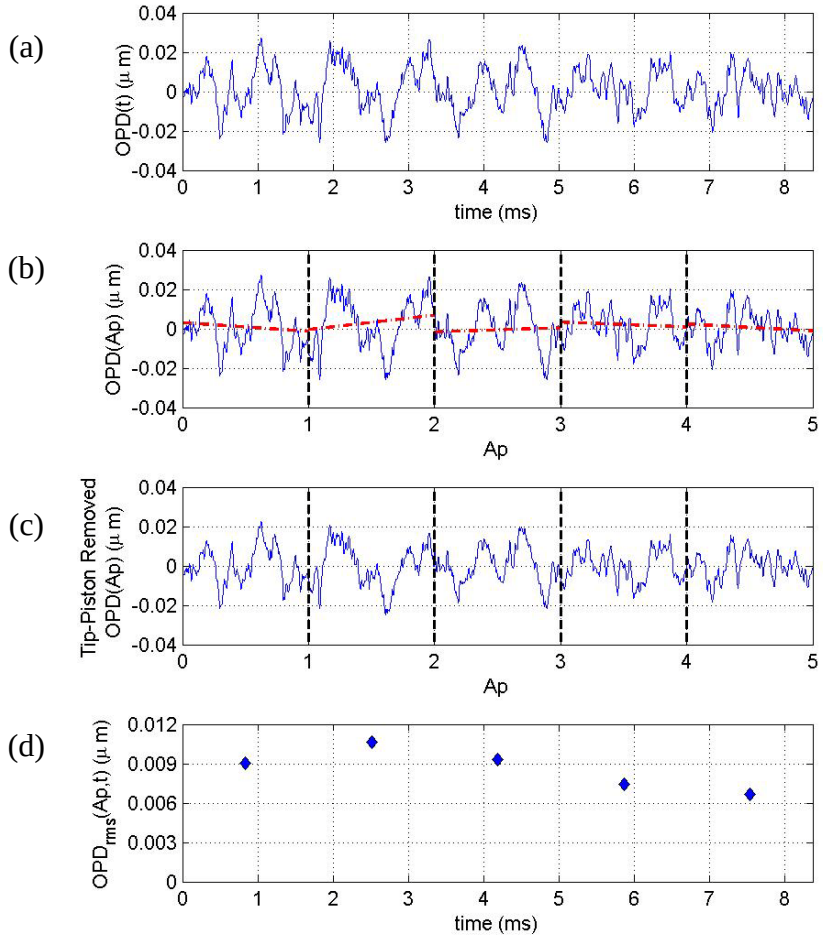

Figure 3. (a) *OPD(t)* calculated from jitter time trace using equation (4), (b) *OPD* divided into blocks in space corresponding to an aperture with the tip-piston across the aperture indicated by the red dashed line, (c) Tip-piston removed *OPD(t;Ap)* and (d) $OPD_{\text{rms}}(t;Ap)$ calculated from the *OPD(t;Ap)* time series.

B. Spatial-Temporal OPD distribution

Let us define a normalized, aperture-dependent wavefront as

$$OPD_{norm}(x,t;Ap) = \frac{OPD(x,t;Ap)}{OPD_{rms}(Ap=\infty)} \tag{6}$$

where the wavefront is normalized by the "infinite-aperture", time-averaged value of the $OPD_{\rm rms}$. Figure 4 shows the probability density function (PDF) of $OPD_{\rm norm}(x)$ for three aperture sizes at M= 0.4 and 0.5. $OPD_{\rm norm}$ is normalized by the spatial time-averaged root-mean-square of $OPD_{\rm norm}$, denoted as μ. From (6) it follows that $\mu(Ap) = \frac{\overline{OPD_{rms}(Ap)}}{OPD_{rms}(Ap=\infty)}$, thus, it depends on the aperture size only. It is clear from Figure 4 that within the range of analyzed aperture sizes, $OPD_{\rm norm}(x)$ has a normal distribution regardless of the aperture size.

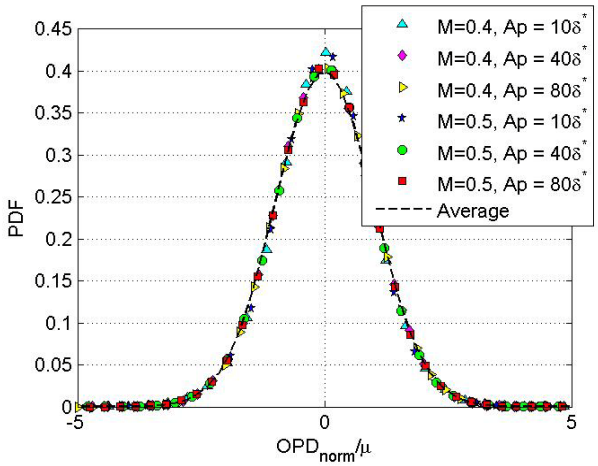

Figure 4. PDF for the $OPD_{\rm norm}(x)$ at M = 0.4 and 0.5 and three aperture sizes plotted as the probability distribution of $OPD_{\rm norm}/\mu$.

If the optical wavefront has a normal distribution in space over the aperture, then the Maréchal formula [24] to calculate the instantaneous Strehl Ratio was shown to be exact for any $OPD_{\rm rms}$ [25],

$$SR(t) = \exp\left(-\left[\frac{2\pi OPD_{rms}(t)}{\lambda}\right]^2\right) \tag{7}$$

Thus, for subsonic boundary layers the instantaneous Strehl Ratio, $SR(t)$, is directly related to the instantaneous $OPD_{\rm rms}(t)$.

C. Temporal $OPD_{\rm rms}$ distribution

Figure 5 shows as a representative example of $OPD_{\rm rms}(t)$ calculated for the aperture of $80\delta^*$ at Mach number of 0.5 and the corresponding instantaneous Strehl ratio, $SR(t)$, computed two different boundary layer thicknesses using the scaling equation (2) and the Maréchal formula (7). Evident from this time traces is that the instantaneous optical aberrations and the instantaneous Strehl Ratio fluctuate significantly about the mean value. Occasionally the fluctuations are noticeably larger, such as the spike at 240 ms in Figure 5, top plot and the corresponding drop-out in Strehl Ratio in Figure 5, bottom plot; these sudden, short-lived spikes are believed to be related to large-scale coherent structures present in the boundary layer [5].

Time traces of $OPD_{\rm rms}(t)$ are not particularly helpful, rather the statistical distribution of $OPD_{\rm rms}(t)$ in time is more relevant. Figure 6, left plot, shows a probability density function for the $OPD_{\rm rms}(t)$ for the aperture of $80\delta^*$ for M = 0.4 and 0.5. The shape of the PDF at each Mach number is well-approximated by a log-normal probability density function,

$$PDF(OPD_{rms}) = \frac{1}{OPD_{rms}\, s\sqrt{2\pi}} \exp\left[-\frac{\left(\ln(OPD_{rms}) - m\right)^2}{2s^2}\right] \tag{8}$$

where *m* is the temporal mean and *s* is the temporal standard deviation of the natural log of $OPD_{rms}(t)$. The dashed lines in Figure 6 are log-normal distributions where the *m* and *s* parameters have been calculated from the experimental data at each Mach number. As these curves show, the log-normal distribution captures the general shape characteristics of the experimental data quite well.

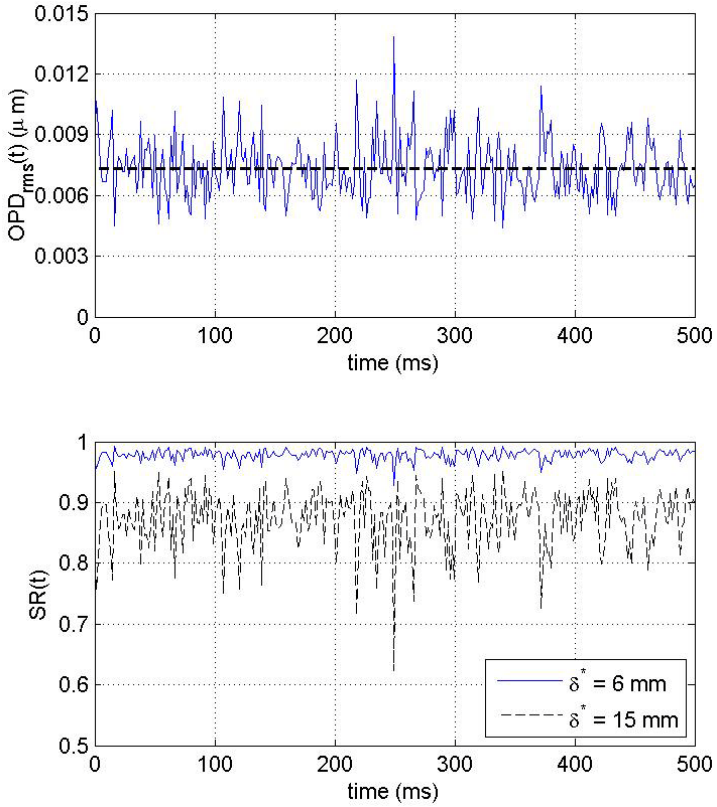

Figure 5. Top: Time trace of OPD_{rms} over an $Ap = 80\delta^*$ aperture, M = 0.5. Bottom: the resulting Strehl Ratio for a δ^* = 6 mm and 15 mm.

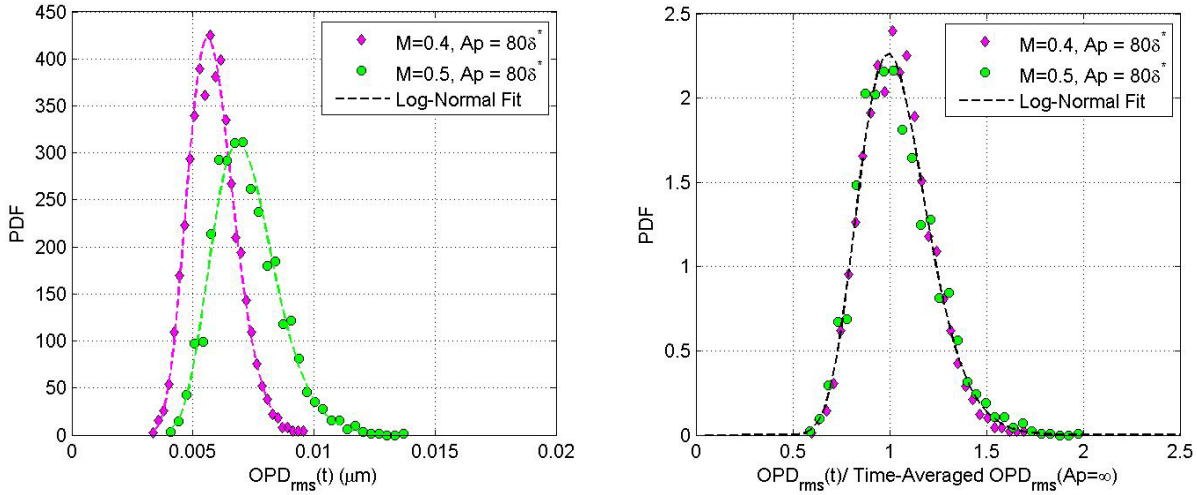

Figure 6. Left: PDF of $OPD_{rms}(t;Ap)$. Right: PDF of the normalized $OPD_{rms}(t;Ap)/\overline{OPD_{rms}(Ap)}$. M= 0.4 and 0.5

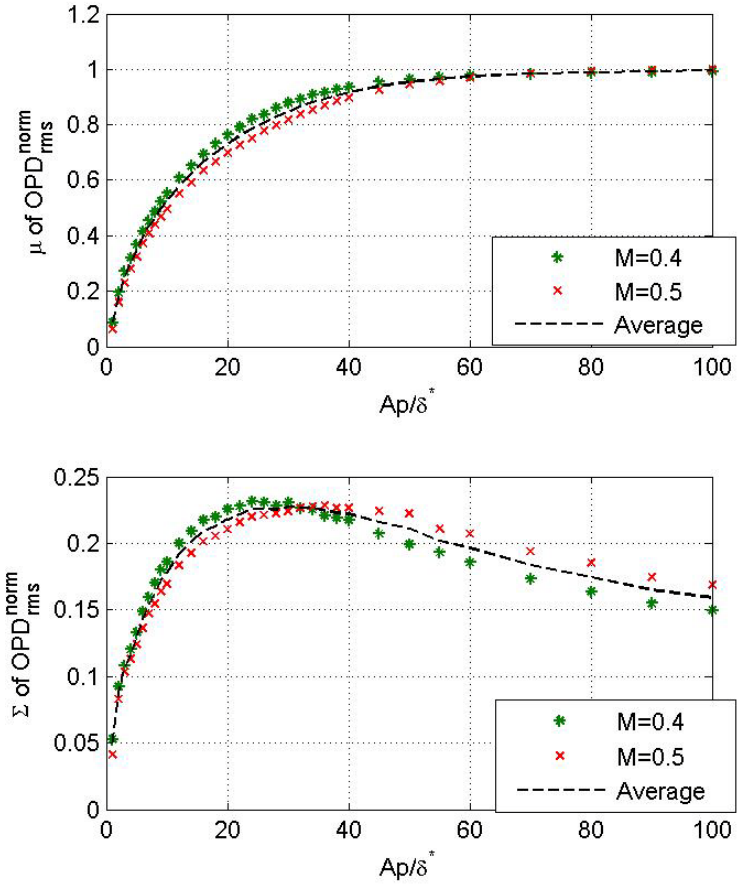

Figure 7. (Top) The temporal mean, μ, and (bottom) the spread, Σ, of $OPD_{rms}^{norm}(t)$ for different aperture size at Mach numbers of 0.4 and 0.5.

Probability distributions of the normalized $OPD_{rms}^{norm}(t)$, equation (6) for M = 0.4 and 0.5 for $Ap = 80\delta^*$ are shown in Figure 6, right plot. The probability density functions for different Mach numbers are now collapsed into a single curve, but the shape of the curve is a function of the aperture, as changing the size of the aperture results in different values of the mean and standard deviation for the normalized $OPD_{rms}^{norm}(t)$. The values of the temporal mean, μ, and the temporal standard deviation or the spread, Σ, of the $OPD_{rms}^{norm}(t)$ versus the aperture size were calculated from experimental data and are shown in Figure 7 for the M = 0.4 and 0.5. The slight variation between the different Mach number curves is not considered significant and likely results from small deviations between the actual δ^* value and the value used in the analysis and/or temperature effects that were neglected. It was shown in [26] that due to tip/tilt-removing effects for finite apertures, when the size of the aperture is increased, the mean value of $OPD_{\text{rms}}(t;Ap)$ approaches the "infinite" aperture value of $\overline{OPD_{rms}(Ap=\infty)}$, or, in other words, μ approaches one; from the experimental data it can be observed that this unity value is achieved when the size of the aperture is larger than 60 δ^*. From the plot of the spread, Σ, of the $OPD_{rms}^{norm}(t)$, Figure 7, bottom plot, the spread initially increases as the aperture size increases, but at approximately $30\delta^*$ the value of Σ begins to decrease. The initial increase is the result of the aperture being smaller than the characteristic size of the optically active structures in the boundary layer; until

several complete optically active structures are within the aperture at a given instance (which occurs at approximately 30 δ^*) the spread will continue to increase with increasing the aperture size. However, once the aperture is larger than the characteristic size of several optically active structures, the spread of $OPD_{\rm rms}(t)$ will decrease. It is anticipated that if the aperture were allowed to continue to increase in size until it was infinitely large, the value of the spread, Σ, would go to zero while the mean value, μ, would become one; thus, for an infinite aperture, the PFD of $OPD_{\rm rms}(t)$ would become the delta-function centered at unity.

The PDF of the $OPD_{rms}^{norm}(t)$, equation (8) can be defined in terms the mean value, μ, and the spread, Σ, which are in turn functions of the aperture size, see Figure 7. These parameters are related to the *m* and *s* parameters in (8) as,

$$m = \log\left(\frac{\mu}{\sqrt{1+(\Sigma/\mu)^2}}\right), \quad s^2 = \log\left(1+(\Sigma/\mu)^2\right) \tag{9}$$

Knowing the PDF of non-dimensional $OPD_{rms}^{norm}(t)$, it is possible to reconstruct the actual PDF of *dimensional* $OPD_{\rm rms}(t)$, equation (8), for any aperture size using (9), the data from Figure 7 and the scaling law for $\overline{OPD_{rms}(Ap=\infty)}$, equations (2) or (3).

D. Instantaneous Strehl Ratio

It is often of interest to find the statistical properties of the instantaneous far-field Strehl Ratio, such as the percentage of time below a certain threshold value, which is directly related to data loss for laser-based communication systems. The Maréchal formula, equation (7), can be rearranged to solve for $OPD_{\rm rms}$ as a function of *SR* as $OPD_{rms}(t) = \frac{\lambda}{2\pi}\sqrt{-\ln[SR(t)]}$, or, it can re-written in terms of the OPD_{rms}^{norm} as,

$$OPD_{rms}^{rms}(t) = \frac{\lambda}{2\pi\overline{OPD_{rms}(Ap=\infty)}}\sqrt{-\ln[SR(t)]} \tag{10}$$

Often, optical communication systems require that the laser signal strength at the far-field receiving station remains above a minimum value, and thus the communication link can only reliably operate when the Strehl Ratio is above a certain threshold value, $TH_{\rm SR}$; this threshold is typically defined as 50%; below this threshold value the link is considered to be broken. Using equation (10), the threshold value, *TH*, can be found as a function of $TH_{\rm SR}$, the laser wavelength, λ, and $\overline{OPD_{rms}(Ap=\infty)}$ as,

$$TH = \frac{\lambda}{2\pi\overline{OPD_{rms}(Ap=\infty)}}\sqrt{-\ln[TH_{SR}]} \tag{11}$$

If the instantaneous value of the normalized OPD_{rms}^{norm} goes *above* the threshold value, *TH*, then the Strehl ratio goes *below* $TH_{\rm SR}$, and the optical communication system is considered inoperable and the data are lost. To determine the amount of data lost at the far-field, or, equivalently, the total percentage of time that the normalized $OPD_{rms}^{norm}(t)$ is above the given threshold value, *TH*, the complementary cumulative distribution function (CCDF) can be used. For the log-normal distribution given by equation (8), the log-normal complementary cumulative distribution function is defined as,

$$CCDF\left(OPD_{rms}^{norm} > TH\right) = 1 - \frac{1}{2} erfc\left(-\frac{\ln(TH) - m}{s\sqrt{2}}\right) \tag{12}$$

where *erfc* is the complementary error function. Figure 8 shows the CCDF, or the percentage of the $OPD_{rms}^{norm}(t)$ signal above the threshold value, *TH*, for different aperture sizes. For example, for the aperture of 80δ*, when the threshold value, *TH*, is less than 0.5, 100% of the optical aberrations are larger than the threshold value, meaning that in the far field the entire signal will be below the required operational Strehl Ratio threshold. Increasing the threshold value allows parts of the $OPD_{rms}^{norm}(t)$ to begin dropping below the threshold, *TH*, permitting part of the signal to reach the far field with an acceptable Strehl Ratio. For large threshold values, *TH* > 1.8, none of the normalized $OPD_{rms}^{norm}(t)$ signal is above the threshold value, meaning that the entire signal is reaching the far field above the threshold Strehl Ratio. It is important to note that this limitation on *TH* is stricter than for average "power-in-the-bucket" applications, for which *TH* >1 is sufficient enough.

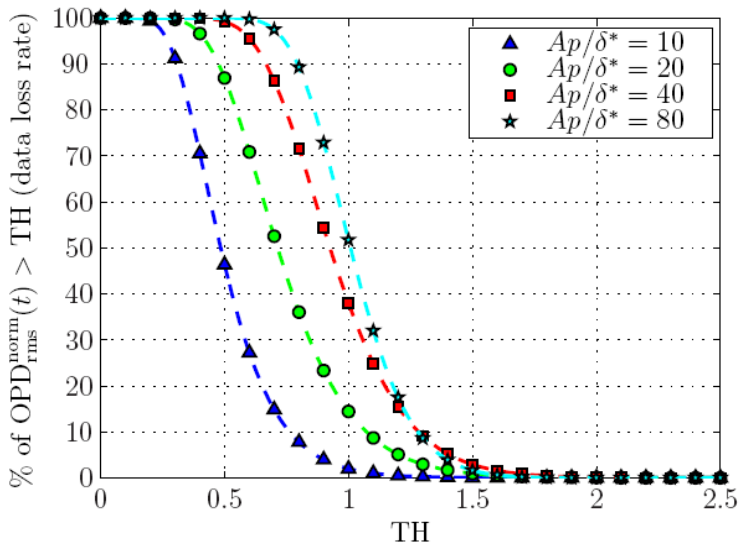

Figure 8. CCDF of a log-normal PDF showing the percentage of $OPD_{rms}^{norm}(t)$ that is above the threshold value versus TH for various aperture sizes.

Summarizing, the percentage of data lost due to boundary-layer aero-optical aberrations for given flight conditions and the aperture size can be estimated as follows:

1. Calculate $\overline{OPD_{rms}(Ap=\infty)}$ for the anticipated boundary layer parameters using equations (2) or (3).
2. Determine the threshold value, *TH*, for $\overline{OPD_{rms}(Ap=\infty)}$, the laser wavelength, λ, and the threshold of Strehl Ratio, TH_{SR}, using equation (11).
3. For the given Ap/δ^* value, find the mean, μ, and the spread, Σ, values from Figure 7.
4. Using equation (9), calculate the *m* and *s* parameters defining the log-normal distribution of the normalized $OPD_{rms}^{norm}(t)$.

5. Calculate the amount of data lost for the given *m*, *s*, and *TH* parameters using the CCDF(*TH*) function, equation (12).

To illustrate the procedure, let us compute the amount data loss for the subsonic boundary layer with the following parameters: the boundary layer thickness of δ = 10 cm (giving the boundary-layer displacement thickness, $\delta^* \sim \delta/8$ = 1.25 cm), M = 0.8, an altitude of 5,000 ft, the viewing angle is normal to the wall and the aperture of $Ap = 80\delta^*$ = 1 m. Using the equation (3) the level of aero-optical distortions would be $\overline{OPD_{rms}(Ap=\infty)}$ = 0.11 μm. For a laser wavelength of λ = 1 μm and the Strehl Ratio threshold of TH_{SR} = 0.5, from equation (11), *TH* can be calculated as 1.2. Finally, Figure 8 gives the amount of lost data as 25%.

IV. Conclusions

The instantaneous aero-optical aberrations caused by subsonic boundary layers were experimentally investigated. The analysis presented in this paper showed that the spatial distribution of $OPD(x)$ over the aperture had a normal distribution. This result confirmed that for optical aberrations caused by the turbulent boundary layer, the on-axis, far-field Strehl Ratio can directly calculated using the Maréchal formula. The $OPD_{\text{rms}}(t)$ distribution was found to be well approximated by a log-normal PDF. Using the log-normal complementary cumulative distribution function, a procedure was developed to determine the percentage of time when the far-field Strehl Ratio is below a prescribed threshold Strehl Ratio as a function of given boundary layer parameters and the laser wavelength.

This analysis has direct implications for communication applications that depend on the instantaneous intensity of the beam in the far-field. Performing this analysis on an actual optical system with given boundary layer conditions would allow a communications engineer to properly size the optical aperture and select the appropriate laser wavelength in order to achieve an acceptable optical system performance. If the desired performance cannot be achieved due to the boundary layer conditions, then this analysis would dictate how the boundary layer must be altered through active or passive control to mitigate the optical aberration effect of the turbulent boundary layer.

Systems that are strictly concerned with delivering high “power-in-the-bucket” at the far-field depend on the average value of *SR* and tend to not be effected by the instantaneous fluctuations in the beam intensity. Communication and data link applications, however, are very sensitive to signal dropouts. A broken data link due to the $SR(t)$ dropping below the threshold value requires that upon reestablishing the connection the lost data be determined and retransmitted. This demonstrates the importance of a consistent, high-quality beam in the far field for communication and data link applications.

As it was shown in this paper, the zero-data-loss requirement poses a stricter limitation on the level of optical aberrations caused by the turbulent boundary layer that an optical communication system can tolerate; it requires not only the mean value of OPD_{rms} but also the maximum value of $OPD_{\text{rms}}(t)$, for a given aperture, to be below a certain threshold. All of the presented analysis is based upon the frozen flow assumption, and ignores the spatial development of the boundary layer. While this is a safe assumption for smaller apertures, it might lead to incorrect predictions for very large apertures when the boundary layer thickness changes significantly across the aperture. It also neglects any spanwise variation in the optical aberration, but as was shown in [5], two-dimensional wavefront aberrations were also correctly predicted by equation (2) and the

aperture correction. Therefore, any spanwise aperture effects should not greatly affect the statistical results presented in this paper.

Due to high spatial and temporal content of these boundary-layer-related aero-optical aberrations, they are beyond the capabilities of current adaptive-optic systems to correct. Thus, the only practical way to mitigate boundary-layer aero-optical effects is to continue studying the fundamental physical mechanism behind boundary-layer aero-optical distortions, especially the origin of large intensity drop-outs. Once the specific structures in the boundary layer are identified it may be possible to modify their presence and/or character so that their aero-optical effects can be mitigated with flow-control strategies, like the wall cooling, for instance [5].

Acknowledgments

This work was funded by AFOSR, Grant FA9550-09-1-0449. The U.S. Government is authorized to reproduce and distribute reprints for government purposes notwithstanding any copyright notation thereon.

References

[1] Gordeyev S, Jumper EJ. 2010. Fluid dynamics and aero-optics of turrets. Prog. Aerospace Sci. **46**:388–400

[2] Gilbert KG, Otten LJ. eds. 1982. Aero-Optical Phenomena, Progress in Astronautics and Aeronautics, Vol. **80**. New York: AIAA. 412 pp.

[3] Jumper EJ, Fitzgerald EJ. 2001. Recent advances in aero-optics. *Prog. Aerospace Sci.* **37**:299–339

[4] Goodman JW. 2005. *Introduction to Fourier Optics*. Roberts & Company, Englewood, CO, 3rd edition

[4] Gordeyev S, Jumper E, Ng T, Cain A. 2003. Aero-optical characteristics of compressible, subsonic turbulent boundary layer. AIAA Paper 2003-3606

[5] Cress JA. 2010. *Optical aberrations caused by coherent structures in a subsonic, compressible, turbulent boundary layer*. Ph.D. Thesis, Univ. of Notre Dame, Notre Dame, IN

[6] Liepmann HW. 1952. Deflection and diffusion of a light ray passing through a boundary layer. *Tech. Rep. SM-14397*, Douglas Aircraft Company, Santa Monica Division, Santa Monica, CA.

[7] Stine HA, Winovich W. 1956. Light diffusion through high-speed turbulent boundary layers. *Research Memorandum A56B21*, NACA, Washington.

[8] Sutton GW. 1969. Effects of turbulent fluctuations in an optically active fluid medium. *AIAA J.* **7**(9):1737-43.

[10] Sutton GW. 1985. Aero-optical foundations and applications. *AIAA J.* **23**(10):1525–37.

[11] Smits, AJ & Dussauge JP. 1996. *Turbulent Shear Layers in Supersonic Flow*. American Institute of Physics. 357 pp.

[12] Morkivin MV. 1962. Effects of compressibility on turbulent flows. In *Mechanique de la Turbulence*, ed. A. Favre, CNRS, pp. 367–380. Paris, France.

[13] Rose WC. 1979. Measurements of aerodynamic parameters affecting optical performance. Air Force Weapons Laboratory Final Report AFWL-TR-78-191, Kirtland AFB, NM

[14] Gilbert, K.G., "KC-135 Aero-Optical Boundary-Layer/Shear-Layer Experiments," *Aero-Optical Phenomena*, Eds. K.G. Gilbert and L.J. Otten, Vol. 80, *Progress in Astronautics and Aeronautics*, AIAA, New York, 1982, pp. 306-324.

[15] Masson, B., J. Wissler, and L. McMackin, "Aero-Optical Study of a NC-135 Fuselage Boundary Layer," AIAA Paper 94-0277, January 1994.
[16] Gordeyev S, Hayden T, Jumper E. 2007. Aero-Optical and Flow Measurements Over a Flat-Windowed Turret. *AIAA J*, **45**(2), pp. 347-357.
[17] Gordeyev S, Jumper EJ, Hayden T. 2011. Aero-Optics of Supersonic Boundary Layers. AIAA Paper 2011-1325.
[18] Buckner A, Gordeyev S. Jumper E. 2006. Conditional Measurements of Optically-Aberrating Structures in Transonic Attached Boundary Layers. AIAA Paper 2006-0079
[19] Wittich D, Gordeyev S, Jumper E. 2007. Revised Scaling of Optical Distortions Caused by Compressible, Subsonic Turbulent Boundary Layers**.** AIAA Paper 2007-4009
[20] Cress J, Gordeyev S, Jumper E. 2008. Aero-Optical Measurements in a Turbulent, Subsonic Boundary Layer at Different Elevation Angles. AIAA Paper 2008-4214
[21] Wyckham CM, Smits AJ. 2009. Aero-optic distortion in transonic and hypersonic turbulent boundary layers. *AIAA J.* **47**(9):2158–68
[22] Cress J, Gordeyev S, Jumper E. 2010. Aero-Optical Measurements in a Heated, Subsonic, Turbulent Boundary Layer, AIAA Paper 2010-0434
[23] Malley M, Sutton GW, Kincheloe N. 1992. Beam-Jitter Measurements for Turbulent Aero-Optical Path Differences, *Applied Optics*, **31**, pp. 4440-4443.
[24] Mahajan V. 1983. Strehl ratio for aberration in terms of their aberration variance. *Journal of the Optical Society of America*, **73**(*6*), pp.860–861
[25] Ross TS. 2009. Limitations and applicability of the Maréchal approximation. *Applied Optics*, **48**(*10*), pp.1812–1818
[26] Siegenthaler JP. 2010. *Guidelines for Adaptive-Optic Correction Based on Aperture Filtration*. PhD thesis, University of Notre Dame, Notre Dame, Notre Dame, IN